International Journal of Medical, Medicine and Health Sciences
ISSN: 2517-9969
Vol:6, No:3, 2012

# Rigorous Electromagnetic Model of Fourier Transform Infrared (FT-IR) Spectroscopic Imaging Applied to Automated Histology of Prostate Tissue Specimens

Rohith K Reddy[1,2], David Mayerich[1], Michael Walsh[1,2,5], P Scott Carney[1,3] and Rohit Bhargava[1,2,3,4]

*Abstract*—Fourier transform infrared (FT-IR) spectroscopic imaging is an emerging technique that provides both chemically and spatially resolved information. The rich chemical content of data may be utilized for computer-aided determinations of structure and pathologic state (cancer diagnosis) in histological tissue sections for prostate cancer. FT-IR spectroscopic imaging of prostate tissue has shown that tissue type (histological) classification can be performed to a high degree of accuracy [1] and cancer diagnosis can be performed with an accuracy of about 80% [2] on a microscopic ($\approx 6\mu m$) length scale. In performing these analyses, it has been observed that there is large variability (more than 60%) between spectra from different points on tissue that is expected to consist of the same essential chemical constituents. Spectra at the edges of tissues are characteristically and consistently different from chemically similar tissue in the middle of the same sample. Here, we explain these differences using a rigorous electromagnetic model for light-sample interaction. Spectra from FT-IR spectroscopic imaging of chemically heterogeneous samples are different from bulk spectra of individual chemical constituents of the sample. This is because spectra not only depend on chemistry, but also on the shape of the sample. Using coupled wave analysis, we characterize and quantify the nature of spectral distortions at the edges of tissues. Furthermore, we present a method of performing histological classification of tissue samples. Since the mid-infrared spectrum is typically assumed to be a quantitative measure of chemical composition, classification results can vary widely due to spectral distortions. However, we demonstrate that the selection of localized metrics based on chemical information can make our data robust to the spectral distortions caused by scattering at the tissue boundary.

*Keywords*—Infrared, Spectroscopy, Imaging, Tissue classification

## I. Introduction

Mid-infrared spectroscopy has been used extensively to measure the chemical composition of specimens [3]. The vibrational modes of molecules resonate with incident light at specific frequencies and a pattern of absorption can be created by analyzing the response of the specimen at a range of infrared frequencies. These vibrational modes are characteristic of the chemical composition and the mid-infrared spectrum of absorption is hypothesized to contain information that will allow the determination of cell type and disease state of the tissue. Combining infrared microscopy with FT-IR spectroscopy is a relatively recent development and has led to the emergence of FT-IR spectroscopic imaging.[4]

Data acquired from FT-IR spectroscopic imaging can be represented as a three dimensional cube where the $x-y$ plane corresponds to images similar to those from an optical microscope, with the $z$ axis containing the infrared spectrum of the specimen under consideration. Therefore, we know the mid-infrared spectrum at every point in the $x-y$ image and this spectrum is processed to make inferences about the image. There are a few important differences between FT-IR spectroscopic imaging and conventional microscopy. Firstly, no external dyes are needed and the contrast in images is directly obtained from the chemical differences in tissue. Secondly, each pixel in the visible image contains RGB values but in IR imaging contains several thousand values across a bandwidth (2000 to 14000nm) that is about 40 times larger than the visible spectrum. This has potentially greater information compared to microscopy and extracting this information is a subject of current research.

Prostate cancer is among the leading causes of cancer-related deaths among men in the United States. The challenge in cancer research and practice is to provide accurate, objective and reproducible decisions. In both cases, conventional optical microscopy followed by manual examination and recognition based on morphology has been demonstrated to be inadequate for this task.[2] One recent development in this field is the use of FT-IR spectroscopic imaging which uses chemical, rather than morphologic information for diagnosis.[2]

A fundamental assumption in mid-infrared spectroscopy has been that the measured spectrum is a function of the chemical composition alone. This assumption is justified in the analysis of homogeneous samples consisting of a single molecular species. However, the assumption breaks down in spatially heterogeneous, chemically diverse samples, like for example in human tissue. Spectroscopic imaging provides spatially resolved spectra and is useful primarily in samples where there is a non-uniform spatial distribution of chemical species. Therefore, it is important to understand the relation between the chemical composition of a sample, the spatial distribution of chemical species in that sample and the recorded data.

[1]Beckman Institute for Advanced Science and Technology, University of Illinois at Urbana-Champaign, Urbana, IL, USA.
[2]Department of Bioengineering, University of Illinois at Urbana-Champaign, Urbana, IL, USA.
[3]Department of Electrical Engineering, University of Illinois at Urbana-Champaign, Urbana, IL, USA.
[4]Department of Mechanical Engineering, University of Illinois at Urbana-Champaign, Urbana, IL, USA.
[5]Carle Foundation Hospital, Urbana, IL, USA

This understanding is vital to the interpretation of spectra from mid-infrared spectroscopic imaging. In this work, we use a rigorous electromagnetic model based on coupled wave analysis to understand the relation between spectra, chemistry, and the shapes of samples. This general approach has been used previously in other problems [5] but has only recently been applied to microspectroscopy.[6], [7], [8] It has been empirically observed that spectra from the edges of tissues are characteristically distorted from chemically similar tissue in the middle of the same sample. We apply this model to the analysis of epithelial prostate tissue and explain these spectral differences using our model.

We then perform classification of tissue samples and demonstrate that a first-order piecewise-linear correction combined with the selection of robust spectral features can be used to successfully classify tissue types despite these spectral distortions. The tissue type identification and cancer diagnosis are essentially classification problems. Here, the classification problem has been formulated as a supervised learning problem in which several million pixels of accurately labeled data are available for model training and validation.

## II. Theoretical Model

The general optical setup for the spectroscopic imaging system working in transmission mode is shown in figure 1. Cassegrain 1 focuses infrared light on to the sample and light emerging for the opposite end of the sample is collected by cassegrain 2. The sample is assumed to be a linear system consisting of multiple layers of varying (complex) refractive indices. We separate the problem into the transition between pairs of homogeneous layers and transition between homogeneous and heterogeneous layers.

For homogeneous layers' interface, since the system is linear, the electromagnetic field can be described as consisting of a linear combination of plane waves each of which satisfy Maxwell's equations at the boundaries. We identify the response of the system to a single plane wave and finally obtain the total response as a sum of each of these individual responses. The electric (**E**) and magnetic (**H**) fields at a position $\mathbf{r} = (x, y, z)^T$ are represented by their complex amplitudes. The permittivity and permeability of free space are denoted by $\epsilon_0$ and $\mu_0$ respectively. The real and imaginary parts ($n(\bar{\nu})$ and $k(\bar{\nu})$) of the refractive index of each layer can vary with $\bar{\nu}$, the free space wavenumber. Each plane wave can be described by Eqn.1

$$\mathbf{E}(\mathbf{r}, \bar{\nu}, t) = \mathbf{E}_0 \exp(i2\pi\bar{\nu}\mathbf{s}.\mathbf{r}) \quad (1)$$

$$\mathbf{H}(\mathbf{r}, \bar{\nu}, t) = \sqrt{\frac{\epsilon_0}{\mu_0}}(\mathbf{s} \times \mathbf{E}_0) \exp(i2\pi\bar{\nu}\mathbf{s}.\mathbf{r}) \quad (2)$$

where $\mathbf{s} = (s_x, s_y, s_z)^T$

$$s_x^2 + s_y^2 + s_z^2 = \epsilon(\bar{\nu}) = [n(\bar{\nu}) + ik(\bar{\nu})]^2 \quad (3)$$

The temporal dependance of the fields is not explicitly stated here for convenience. In each layer, the electric field can be decomposed into a sum of plane waves (angular spectrum) via the Fourier transform. The field in the $m^{th}$ layer between

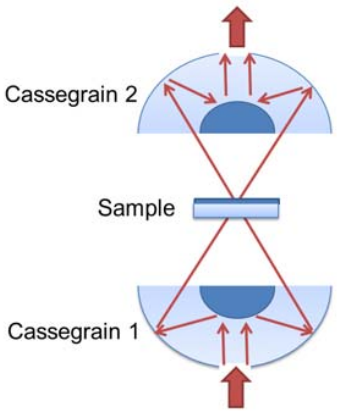


Fig. 1. General instrument setup for transmission mode spectroscopic imaging

$z^{(m-1)}$ and $z^{(m)}$ is given by

$$\begin{aligned}\mathbf{E}^{(m)}(x, y, z, \bar{\nu}) = \bar{\nu} \int\int ds_x ds_y \exp\{i2\pi\bar{\nu}(s_x x + s_y y)\} \\ [\quad B^{(m)}(s_x, s_y, \bar{\nu}) \exp\{i2\pi\bar{\nu}s_z^{(m)}(z - z^{(m-1)})\} \\ +\quad \hat{B}^{(m)}(s_x, s_y, \bar{\nu}) \exp\{-i2\pi\bar{\nu}s_z^{(m)}(z - z^{(m)})\}] \quad (4)\end{aligned}$$

where $s_z^{(m)} = \sqrt{[n^{(m)}(\bar{\nu}) + ik^{(m)}(\bar{\nu})]^2 - s_x^2 - s_y^2}$. The boundary conditions that relate the fields at the top and bottom of a boundary are governed by Maxwell's equations. Using Gauss' Law for electricity, $\nabla \cdot \mathbf{E}(\mathbf{r}, \bar{\nu}) = 0$ we obtain

$$\begin{aligned}s_x B_x^{(m)}(s_x, s_y, \bar{\nu}) + s_y B_y^{(m)}(s_x, s_y, \bar{\nu}) \\ + s_z B_z^{(m)}(s_x, s_y, \bar{\nu}) = 0 \quad (5)\\ s_x \hat{B}_x^{(m)}(s_x, s_y, \bar{\nu}) + s_y \hat{B}_y^{(m)}(s_x, s_y, \bar{\nu}) \\ - s_z \hat{B}_z^{(m)}(s_x, s_y, \bar{\nu}) = 0 \quad (6)\end{aligned}$$

Faraday's law and Ampere's law would require that the transverse components of the electric and magnetic field must be continuous. Consequently,

$$\begin{aligned}B_x^{(m)} \exp(i2\pi\bar{\nu}s_z^{(m)}(z - z^{(m-1)})\}) + \hat{B}_x^{(m)} = \\ B_x^{(m+1)} + \hat{B}_x^{(m+1)} \exp(-i2\pi\bar{\nu}s_z^{(m+1)}(z - z^{(m+1)})\}) \quad (7)\\ B_y^{(m)} \exp(i2\pi\bar{\nu}s_z^{(m)}(z - z^{(m-1)})\}) + \hat{B}_y^{(m)} = \\ B_y^{(m+1)} + \hat{B}_y^{(m+1)} \exp(-i2\pi\bar{\nu}s_z^{(m+1)}(z - z^{(m+1)})\}) \quad (8)\end{aligned}$$

$$\begin{aligned}(s_y B_z^{(m)} - s_z^{(m)} B_y^{(m)}) \exp(i2\pi\bar{\nu}s_z^{(m)}(z - z^{(m-1)})\}) \\ +\quad (s_y \hat{B}_z^{(m)} - s_z^{(m)} \hat{B}_y^{(m)}) = (s_y B_z^{(m+1)} - s_z^{(m+1)} B_y^{(m+1)}) \\ +\quad (s_y \hat{B}_z^{(m+1)} - s_z^{(m+1)} \hat{B}_y^{(m+1)}) \\ \times\quad \exp(-i2\pi\bar{\nu}s_z^{(m+1)}(z - z^{(m+1)})\}) \quad (9)\\ (s_z^{(m)} B_x^{(m)} - s_x B_z^{(m)}) \exp(i2\pi\bar{\nu}s_z^{(m)}(z - z^{(m-1)})\}) \\ -\quad (s_z^{(m)} \hat{B}_x^{(m)} + s_x \hat{B}_z^{(m)}) = (s_z^{(m+1)} B_x^{(m+1)} - s_x B_z^{(m+1)}) \\ -\quad (s_z^{(m)} \hat{B}_x^{(m+1)} + s_x \hat{B}_z^{(m+1)}) \\ \times\quad \exp(-i2\pi\bar{\nu}s_z^{(m+1)}(z - z^{(m+1)})\}) \quad (10)\end{aligned}$$

The field at the first layer is determined by the light incident

from cassegrain 1. The light at the input end of the first cassegrain can be assumed to be uniform and the light incident on the sample is directly related to this input via the cassegrain transfer function [9]. The field exiting from the last ($L^{th}$) layer exits via cassegrain 2 and does not come back. Therefore,

$$\hat{B}_x^{(L)}(s_x, s_y, \bar{\nu}) = 0 = \hat{B}_y^{(L)}(s_x, s_y, \bar{\nu}) = \hat{B}_z^{(L)}(s_x, s_y, \bar{\nu}) \quad (11)$$

The above set of equations completely describes the interaction of the sample and light at the boundary of a pair of homogeneous layers. Knowing the refractive indices and thicknesses of each layer would allow us to completely solve the system of equations. Therefore, the electric and magnetic fields at every point in the sample can be determined. The field on a detector is a magnified version of the field exiting cassegrain 2 and the total light intensity ($\mathbf{I}(\bar{\nu})$) at the detector is the square the field on the detector.

Now consider a homogeneous-heterogeneous layer boundary. The region of transverse heterogeneity is assumed to be of finite area and therefore we can approximate the structure of the object by its two dimensional Fourier series. Each layer is characterized by its complex refractive index or equivalently its permittivity (3). Truncating the Fourier series to a finite number of coefficients gives

$$\epsilon(x, y, \bar{\nu}) \approx \sum_{p=-N_U}^{N_U-1} \sum_{q=-N_W}^{N_W-1} \phi_{p,q}(\bar{\nu}) \exp[i(pUx + qWy)] \quad (12)$$

The periodic nature of the sample implies that the spatial frequencies after scattering are restricted to shifts from the incident frequency by integer multiples of frequencies (constants) $U$ and $W$.

$$u_p = pU + \delta \quad (13)$$
$$w_q = qW + \sigma \quad (14)$$

Each component of the electric and magnetic field can be written in a Fourier decomposition of the form

$$\mathbf{E}^{(m)}(x, y, z, \bar{\nu}) = \sum_p \sum_q \begin{pmatrix} X_{p,q}(z, \bar{\nu}) \\ Y_{p,q}(z, \bar{\nu}) \\ Z_{p,q}(z, \bar{\nu}) \end{pmatrix} \times \exp[i(u_p x + w_q y)] \quad (15)$$

$$\mathbf{H}^{(m)}(x, y, z, \bar{\nu}) = \sqrt{\frac{\epsilon_0}{\mu_0}} \sum_p \sum_q \begin{pmatrix} I_{p,q}(z, \bar{\nu}) \\ J_{p,q}(z, \bar{\nu}) \\ K_{p,q}(z, \bar{\nu}) \end{pmatrix} \times \exp[i(u_p x + w_q y)] \quad (16)$$

Maxwell's equations relate $\mathbf{E}(x, y, z, \bar{\nu})$ and $\mathbf{H}(x, y, z, \bar{\nu})$ giving

$$\nabla \times \mathbf{E}(x, y, z, \bar{\nu}) = i2\pi\bar{\nu}\sqrt{\frac{\mu_0}{\epsilon_0}}\mathbf{H}(x, y, z, \bar{\nu}) \quad (17)$$

$$\nabla \times \mathbf{H}(x, y, z, \bar{\nu}) = -i2\pi\bar{\nu}\sqrt{\frac{\epsilon_0}{\mu_0}}\epsilon(x, y, z, \bar{\nu})\mathbf{E}(x, y, z, \bar{\nu}) \quad (18)$$

Expanding the above equations using Eqn.15 and Eqn.16 yields

$$\frac{dX_{p,q}(z, \bar{\nu})}{dz} = i2\pi\bar{\nu}J_{p,q}(z, \bar{\nu}) + iu_p Z_{p,q}(z, \bar{\nu}) \quad (19)$$
$$\frac{dY_{p,q}(z, \bar{\nu})}{dz} = -i2\pi\bar{\nu}I_{p,q}(z, \bar{\nu}) + iw_q Z_{p,q}(z, \bar{\nu}) \quad (20)$$

$$\frac{dK_{p,q}(z, \bar{\nu})}{dz} = 1/(i2\pi\bar{\nu})[u_p Y_{p,q}(z, \bar{\nu}) - w_q X_{p,q}(z, \bar{\nu})] \quad (21)$$

$$\frac{dI_{p,q}(z, \bar{\nu})}{dz} = -i2\pi\bar{\nu} \sum_{p',q'} \phi_{p-p',q-q'}(\bar{\nu}) Y_{p',q'}(z, \bar{\nu}) + iu_p K_{p,q}(z, \bar{\nu}) \quad (22)$$

$$\frac{dJ_{p,q}(z, \bar{\nu})}{dz} = i2\pi\bar{\nu} \sum_{p',q'} \phi_{p-p',q-q'}(\bar{\nu}) X_{p',q'}(z, \bar{\nu}) + iu_p K_{p,q}(z, \bar{\nu}) \quad (23)$$

$$\frac{dK_{p,q}(z, \bar{\nu})}{dz} = -1/(i2\pi\bar{\nu}) \sum_{p',q'} \phi_{p-p',q-q'}(\bar{\nu}) \times [u_{p'} J_{p',q'}(z, \bar{\nu}) - w_{q'} I_{p',q'}(z, \bar{\nu})] \quad (24)$$

These equations can be organized in the form of a matrix differential equation.

$$\begin{pmatrix} \frac{dX(z,\bar{\nu})}{dz} \\ \frac{dY(z,\bar{\nu})}{dz} \\ \frac{dI(z,\bar{\nu})}{dz} \\ \frac{dJ(z,\bar{\nu})}{dz} \end{pmatrix} = i2\pi\bar{\nu}\Delta \begin{pmatrix} X(z, \bar{\nu}) \\ Y(z, \bar{\nu}) \\ I(z, \bar{\nu}) \\ J(z, \bar{\nu}) \end{pmatrix} \quad (25)$$

The above above matrix equation couples the electric and magnetic fields. We can decouple these equations by computing the eigenvalues and eigenvectors of $\Delta = G\Lambda G^{-1}$. Consequently, we can find $X(z, \bar{\nu}), Y(z, \bar{\nu}), I(z, \bar{\nu}), J(z, \bar{\nu})$ in terms of the eigenvalues and eigenvectors. Using boundary conditions of the form in Eqns.7-10, we can find the fields $\mathbf{E}^{(m)}(x, y, z, \bar{\nu})$ and $\mathbf{H}^{(m)}(x, y, z, \bar{\nu})$ in every layer $m$.

## III. Bayesian Classification

Classification of tissue types based on spectral signature is performed using a naive Bayes' model. Biopsy samples in a commercially-available tissue micro-array (TMA) are imaged using a Perkin-Elmer Spotlight 300 mid-infrared imaging system. Neighboring tissue sections are subjected to a panel of histology stains in order to discern cell type. Spectra associated with specific cell types are then labeled in the mid-infrared image by an experienced pathologist, providing a significant sampling of spectra representing ten different tissue types that are important in prostate diagnosis. The epithelial cell type is particularly important, since epithelial cells are the source of most tumors that occur in the prostate. It is this cell type that is considered in this paper.

After ground-truth spectra are identified, an experienced spectroscopist identifies features in the spectra that can be used to identify these unique classes. These features are selected with a particular focus on making them robust to noise and spectral distortions due to scattering. Each spectral feature is based on two nearby baseline points that are assumed to have zero absorbance due to chemistry. This baseline is used as a

first-order correction to reduce the distortion in the absorbance spectrum due to scattering. Selected features include (a) peak ratios, (b) area under a peak, and (c) the center of gravity under the spectrum between two points.

The posterior probability and prior probabilities are determined using the training set, which consists of a ground-truth class and feature vector for each spectrum. This allows the computation of the joint posterior probability $p(C|\mathbf{x})$, which is used to select the class for any input spectrum. This technique has been demonstrated for mid-infrared classification in tissue samples previously, [1] achieving an average area under the receiver operating characteristic curve of 0.991 for epithelium.

## IV. Results

In this section, we simulate the distortions found at the interface of epithelial tissue with air placed on a homogeneous barium fluoride substrate. The raw absorbance spectrum for epithelial tissue is derived from mid-infrared spectroscopic images far away from an interface that causes spectral distortions. The imaginary component of the refractive index is derived from this spectrum via Eqn. 26. Here $\rho$ is the concentration of the absorbing species and is taken to be unity since there is only one species. The real part of refractive index is then computed via Kramers-Kronig relations.

$$a(\bar{\nu}) = 4\pi\nu k(\bar{\nu})/(2.303\rho) \tag{26}$$

The specimen absorbance is computed at several intervals on either side of the epithelium-air interface (Fig. 2). The epithelial layer thickness is 10 $\mu m$ and the barium fluoride layer is assumed to be 2 $mm$. The complex refractive index of epithelium is used to create a heterogeneous layer with an edge at $d = 0$ and this heterogeneous layer is decomposed into its Fourier series according to Eqn. 12. Twenty Fourier coefficients were used to represent the edge and the shape of this edge is as shown in Figure 2. It may be noted from Figure 2 that spectral distortions in the higher-wavenumber regions of the spectra increase as the interface is approached from within the epithelium tissue region. These distortions are significant at edges and the absorbance values can vary as much as 60%. It is important to note that these spectral differences are not because of chemical differences (since we have only one absorbing chemical species, namely, epithelium), but due to optical effects alone. In FT-IR imaging it has been fundamentally assumed that spectral differences are due to chemistry alone. These spectral results indicate the dependance of spectral data on the shape of the object (i.e. the presence of an edge). Moreover, there is a predictable relation between the position at which light is incident and the shape of the spectrum that can be calculated using our model.

A prostate tissue biopsy core from a TMA is imaged and spectral samples are shown from epithelial tissue selected by a pathologist. Spectral samples are taken at varying distances from an edge and plotted in Figure 3. Note the comparable distortions found in both the experimental and simulated spectra. We then compute the feature vector $\mathbf{x_i}$ corresponding to each simulated spectrum (Sec. III) and perform classification using the Naive Bayes classifier. The joint posterior probability

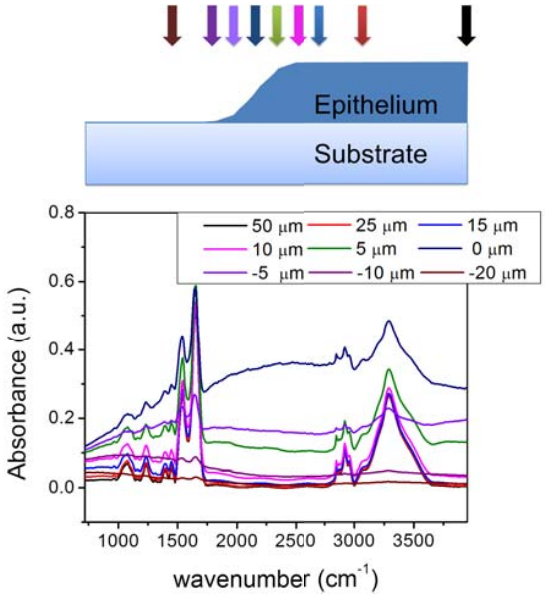


Fig. 2. Spectral distortions at specified distances from the epithelium-substrate interface. Positive values indicate spectra taken from epithelial tissue. Negative values indicate spectra taken from a homogeneous barium fluoride substrate. A distance of $d = 0$ indicates the center position of the interface.

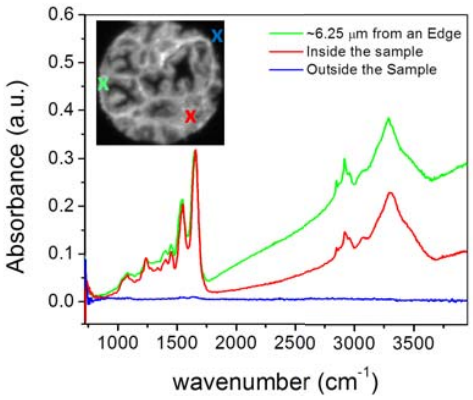


Fig. 3. Scattering distortions shown for spectral samples taken from experimental data. The inset shows a ≈1mm prostate biopsy core imaged with a 6.25$\mu$m pixel size and placed on a 2mm barium fluoride slide. Sample spectra are taken at varying distances from the tissue-air interface. Note the significant difference in absorption as the sampled spectra approaches the edge.

is then computed and plotted in Figure 4. The joint posterior probability inferred by the Naive Bayes' classifier implies the presence of epithelium up to and including the interface, but not beyond. Our classifier uses specific spectral metrics as described in section III and also utilizes the fact that air has no spectral signature in the mid-infrared. This demonstrates that the classification is robust to severe distortions introduced into the spectra by scattering caused by nearby edges.

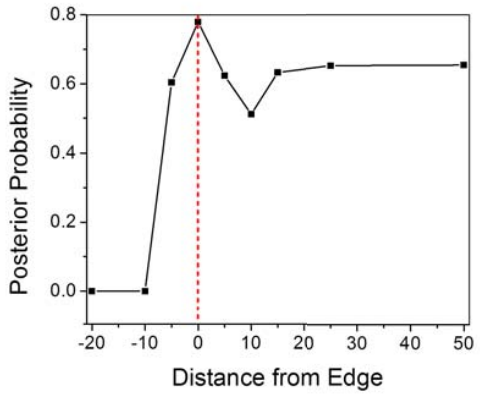


Fig. 4. Joint posterior probability $p(E|\mathbf{x_i})$ of the Bayesian classifier as a function of distance from the epithelium-air interface. The selection of robust metrics and first-order scattering correction is sufficient to properly characterize the tissue class up to the interface (specified by the red line).

## V. Conclusion

In this paper, we propose a model for understanding distortions related to object shape and scattering at object interfaces in mid-infrared spectroscopic images of tissue samples. We show that spectra of epithelial tissue are not only a function of the underlying chemistry as conventionally assumed, but also a function of their proximity to a lateral tissue-air interface. A naive Bayes classifier is trained on spectra labeled by a pathologist using features selected by an expert spectroscopist. These features are selected based on chemical characteristics of the spectra with a particular focus on robustness to distortions. This robustness is demonstrated on simulated data, where spectra simulated up to the epithelium interface are classified with a high joint posterior probability. Automated histological classification of prostate tissue using FT-IR spectroscopic imaging is robust to severe spectral distortions.

## References

[1] D. Fernandez, R. Bhargava, S. Hewitt, and I. Levin, "Infrared spectroscopic imaging for histopathologic recognition," *Nature biotechnology*, vol. 23, no. 4, pp. 469–474, 2005.
[2] R. Bhargava, *Analytical and bioanalytical chemistry*, vol. 389, no. 4, pp. 1155–1169, 2007.
[3] C. Craver, "The coblentz society desk book of infrared spectra," DTIC Document, Tech. Rep., 1977.
[4] E. Lewis, P. Treado, R. Reeder, G. Story, A. Dowrey, C. Marcott, and I. Levin, "Fourier Transform Spectroscopic Imaging Using an Infrared Focal-Plane Array Detector," *Anal. Chem.*, vol. 67, no. 19, pp. 3377–3381, 1995.
[5] M. Moharam and T. Gaylord, *JOSA*, vol. 71, no. 7, pp. 811–818, 1981.
[6] B. Davis, P. Carney, and R. Bhargava, "Theory of midinfrared absorption microspectroscopy: I. homogeneous samples," *Anal. Chem.*, vol. 82, no. 9, pp. 3474–3486, 2010.
[7] ——, "Theory of mid-infrared absorption microspectroscopy: Ii. heterogeneous samples," *Anal. Chem.*, vol. 82, no. 9, pp. 3487–3499, 2010.
[8] R. Reddy, B. Davis, P. Carney, and R. Bhargava, "Modeling fourier transform infrared spectroscopic imaging of prostate and breast cancer tissue specimens," *IEEE International Symposium on Biomedical Imaging*, pp. 738–741, 2011.
[9] B. Richards and E. Wolf, "Electromagnetic diffraction in optical systems. II," *Proceedings of the Royal Society of London. Series A*, vol. 253, no. 1274, pp. 358–379, 1959.